Pulse-length effects in strong-field ionization of atoms by co-rotating and counter-rotating bicircular laser pulses

Mahmoud Abu-samha [1,*] and Lars Bojer Madsen [2,†]

[1] *College of Engineering and Technology, American University of the Middle East, Kuwait*

[2] *Department of Physics and Astronomy, Aarhus University, 8000 Aarhus C, Denmark*

(Received 14 August 2019; published 23 October 2019)

We study strong-field ionization of H and selected rare-gas atoms by solving the three-dimensional time-dependent Schrödinger equation in the single-active-electron approximation with particular attention to the effect of pulse length on the total ionization yields (TIYs) produced by counter-rotating bicircular (CRBC) lasers compared to co-rotating bicircular (COBC) lasers. To this end, TIYs, photoelectron momentum distributions, and above-threshold ionization spectra are presented for various pulse durations and peak intensities. For pulses containing five or more cycles of the fundamental near-infrared laser field, the CRBC/COBC ratio of TIYs is affected due to ionization via excited states and multiphoton ionization channels. For pulses containing less than five cycles, the CRBC/COBC ratio of TIYs depends on both the frequency combination and number of optical cycles: With the 1ω-2ω frequency combination, the ratio of TIYs is enhanced (reduced) for pulses with an odd (even) number of optical cycles. The 1ω-3ω frequency combination was considered for pulses containing two or three optical cycles, and for both pulse lengths the CRBC/COBC ratio of TIYs is less than unity.

DOI: 10.1103/PhysRevA.100.043415

I. INTRODUCTION

In strong-field physics, bicircular laser pulses are produced as a superposition of two circularly polarized laser pulses. The shape of a bicircular laser field depends on the frequency ratio, intensity ratio, and helicities of the combined fields. If the two circular fields are polarized in the same direction, the produced bicircular field is co-rotating. If the two circular fields are polarized in opposite directions, the produced bicircular field is counter-rotating. In the following, we refer to a bicircular field as BC, a counter-rotating bicircular field as CRBC, and a co-rotating bicircular field as COBC.

In recent years, the use of BC laser pulses to explore ionization dynamics and high-order-harmonic generation (HHG) from atoms and molecules in strong laser fields [1–13] has led to breakthroughs in controlling the ionization process [5,6], probing the phase and amplitude of the emitted wave packets [12], and producing circularly polarized extreme ultraviolet high harmonics [13]. Here our focus is strong-field ionization of atoms and molecules by BC pulses, and investigation of the information contents of above-threshold ionization (ATI) spectra and photoelectron momentum distributions (PMDs) produced by such lasers.

To present an overview of recent findings in this research area, we find it useful to start with an example and use that to connect to the recent literature. Figure 1 shows examples of BC fields and corresponding PMDs. The Lissajous patterns shown in Figs. 1(a) and 1(b) correspond to COBC and CRBC fields, respectively, with the 1ω-2ω frequency combination, where $\omega = 0.057$ a.u. corresponds to a wavelength of 800 nm, the intensity ratio is 1:1, and the intensity is 4.5×10^{13} W/cm^2 (one atomic unit of intensity corresponds to 3.51×10^{16} W/cm^2). At these laser parameters, while the COBC field looks similar to a circularly polarized field, the CRBC field shows a three-lobe structure. In strong-field ionization by CRBC and COBC laser fields in the long pulse limit [14], the symmetry of the ionizing field is imprinted in the PMDs in the plane of laser polarization. This can clearly be seen in Figs. 1(c) and 1(d), which include PMDs for atomic hydrogen initially in the $1s$ ground state ionized by 10-cycle COBC and CRBC laser pulses, respectively, based on time-dependent Schrödinger equation (TDSE) calculations (see below). Ionization by a COBC laser leads to crescent-shaped structures in the PMD in Fig. 1(c), similar to emission patterns for H ionized by circularly polarized lasers [15,16]. For ionization by a CRBC laser, the PMD in Fig. 1(d) reveals threefold symmetric structures. The ringlike progressions seen in Figs. 1(c) and 1(d) are caused by multiphoton absorption already occurring with ionizing fields containing 10 cycles. Changes to the frequency ratio or the intensity ratio were investigated in Ref. [14] and the impact on PMDs was addressed. For example, it was found that the number of lobes in the PMDs produced by CRBC lasers depends on the frequency ratio: A CRBC field with a $r\omega$-$s\omega$ frequency ratio produces an emission pattern with $(r + s)$ lobes in the PMDs.

For atoms initially in states with angular momentum quantum number $l > 0$ [take Ar($3p$) as an example] and for aligned molecular targets (such as H_2^+) probed by CRBC lasers, the observation of n-fold symmetric emission patterns in PMDs [as in Fig. 1(d)] depends on the alignment angle, as was shown in a recent theoretical study for H_2^+ [17]: The PMDs of H_2^+ show an n-fold symmetry only when the molecular axis is

*Mahmoud.Abusamha@aum.edu.kw

†bojer@phys.au.dk

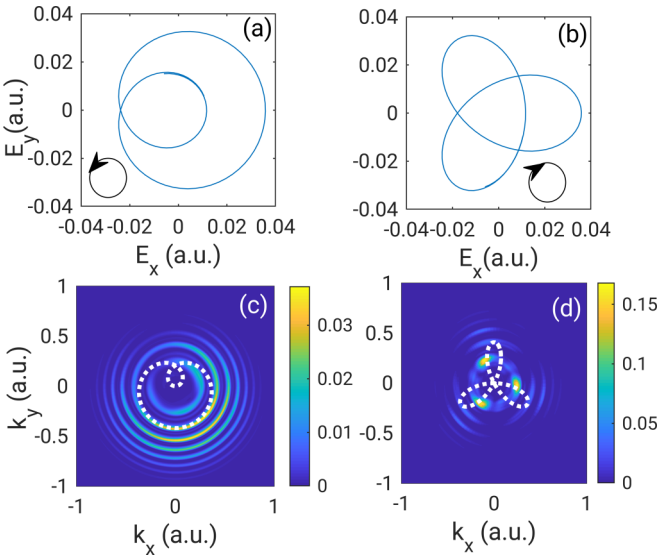

FIG. 1. Lissajous curves of one cycle at the peak electric field for 10-cycle (a) COBC and (b) CRBC laser pulses with the 1ω-2ω frequency combination ($\omega = 0.057$ a.u.) and a laser intensity of 4.5×10^{13} W/cm^2. The COBC field rotates in the anticlockwise direction, whereas the CRBC field rotates in the clockwise direction. The corresponding PMDs from TDSE calculations are included in (c) and (d), along with the predicted final momentum from Eq. (1) (white dotted curves).

aligned perpendicular to the plane of the laser polarization. At this alignment angle, the molecular potential is symmetric in the plane of the laser polarization.

For H ionized by BC pulses [see Figs. 1(c) and 1(d)], ionization by COBC pulses drives the photoelectron to higher momentum values, whereas CRBC pulses produce electrons with significantly lower momenta. This difference has been explained in Ref. [2], where the final electron momentum $\vec{k}_f$ was estimated by

$$\vec{k}_f = -\int_{t_i}^{\infty} \vec{E}(t)dt = -\vec{A}(t_i), \tag{1}$$

where t_i is the instant of ionization, $\vec{E}(t)$ is the electric field, and $\vec{A}(t)$ is the vector potential of the laser pulse at the time of ionization. In this simple model where the ionic potential is neglected, the final momentum is determined from the vector potential $\vec{A}(t)$ of the external field. For ionization by COBC pulses, the electric field has one maximum per laser cycle [see Fig. 1(a)], with a corresponding maximum in the vector potential and the photoelectron will thus be driven to a higher momentum value compared to CRBC pulses. For ionization by CRBC pulses, the electric field has three maxima per laser cycle [see Fig. 1(b)], which corresponds to three minima in the vector potential.

If one takes a closer look at the PMDs in Figs. 1(c) or 1(d), one observes an offset angle between the calculated peak positions in the PMDs and the expected final momentum based on Eq. (1); the latter is shown in Figs. 1(c) and 1(d) as a dotted white curve. In Refs. [17,18], it was found that the offset angle depends on the momentum value: The higher the momentum, the smaller the offset angle. The momentum-dependent offset angle was attributed to ionization time delays for electrons with different continuum energies [18].

While most strong-field studies interrogate PMDs in the plane of laser polarization, essential information regarding the ionization process, including subcycle ionization dynamics and, e.g., signatures of atomic or molecular orbitals, may be contained in the PMDs along the laser propagation direction, as was shown for small molecules in circularly polarized lasers [19,20] and for He in BC lasers [21].

The present study is motivated by recent experiments on strong-field ionization of rare gases [22]. In the experiments, the rare-gas atoms Ar, Kr, and He were ionized by 40 fs BC pulses with various intensity ratios and the 1ω-2ω frequency combination (ω corresponds to 800 nm wavelength). For each rare-gas atom, the study compared the total ionization yields (TIYs) for CRBC and COBC laser pulses and, at intermediate intensities (10^{13}–10^{14} W/cm^2), reported enhancement of TIYs for CRBC lasers compared to COBC lasers. The enhancement of TIYs is very sensitive to laser peak intensity and is partly due to resonance-enhanced multiphoton ionization (REMPI). The dependence of this phenomenon on laser intensity was addressed in Ref. [23] based on the strong-field approximation and Wigner's threshold law [24]: They explained the enhancement of TIYs for the CRBC pulse by pronounced threshold anomalies at the channel closing. These anomalies and channel-closing effects were found to be negligible for COBC pulses.

In this work, we present TDSE calculations of TIYs for H and selected rare-gas atoms (Ar, Ne, and He) probed by CRBC and COBC pulses in a different ionization regime, namely, ionization by BC pulses containing few cycles, and we find that whether to observe an enhancement of TIYs for CRBC over COBC pulses depends on the number of optical cycles and the frequency ratio of the combined fields. In short, for pulses with the 1ω-2ω frequency combination, the enhancement of TIYs for CRBC pulses is observed only for pulses with an odd number of cycles. For laser pulses with an even number of cycles, the TIYs for CRBC pulses are reduced compared to COBC pulses. For pulses with the 1ω-3ω frequency combination, TIYs were computed for two-cycle and three-cycle pulses and, in both cases, the CRBC pulses produce lower TIYs than COBC pulses. This effect is explained in terms of the shape of the ionizing electric field. These findings are also predicted by calculations of TIYs based on tunneling theory. We have also considered the long pulse limit, for which case the TDSE calculations at specific intensities show larger TIYs for CRBC compared to COBC pulses, in agreement with the recent experiments [22].

The computational details are contained in Sec. II, followed by results and discussion in Sec. III and conclusions in Sec. IV. Atomic units (a.u.) are used throughout, unless stated otherwise.

II. COMPUTATIONAL DETAILS

The TDSE methodology has been discussed in details elsewhere [17,25]. In brief, the TDSE is solved for an effective one-electron potential describing the interaction with the nucleus, the remaining electrons, and the external field.

The time-dependent wave function $\psi(\mathbf{r},t)$ is expanded in spherical harmonics $Y_{lm}(\Omega)$ for the angular degrees of freedom and a radial grid for the time-dependent reduced radial wave functions, $f_{lm}(r,t)$, i.e.,

$$\psi(\mathbf{r},t)=\sum_{lm}\frac{f_{lm}(r,t)}{r}Y_{lm}(\Omega). \tag{2}$$

The TDSE is propagated in the velocity gauge [25] with a combined split-operator [26] Crank-Nicolson method.

The vector potential describing CRBC (COBC) laser fields with the 1ω-$s\omega$ frequency combination is defined as

$$\vec{A}(t)=\frac{A_0 f(t)}{\sqrt{2}}\begin{pmatrix}\cos(\omega t+\phi)+\cos(s\omega t+\phi)\\ \sin(\omega t+\phi)+\eta\sin(s\omega t+\phi)\\ 0\end{pmatrix}, \tag{3}$$

with A_0 the amplitude, ω the carrier angular frequency, ϕ the carrier envelope phase (CEP), and $f(t)=\sin^2(\omega t/2N_{\rm cyc})$ the pulse envelope containing $N_{\rm cyc}$ cycles at the fundamental angular frequency. In Sec. III, whenever we refer to an odd or even number of cycles, we refer to the number $N_{\rm cyc}$ in the envelope $f(t)$. Notice that at 800 nm, the duration of a single cycle is 110.2 a.u., corresponding to $\simeq$2.6 fs. In Eq. (3), $\eta=+1$ for COBC pulses and -1 for CRBC pulses. We consider laser pulses with frequency combinations 1ω-2ω and 1ω-3ω. The magnitude of the electric field, $|E(t)|$, with $\vec{E}(t)=-\partial_t\vec{A}(t)$ is plotted in Fig. 2 for COBC (dotted lines) and CRBC (solid lines) fields with the 1ω-2ω frequency combination, a 1:1 intensity ratio, and containing $N_{\rm cyc}=2$–5 optical cycles of the fundamental angular frequency. Figure 2 shows that for an odd number of cycles, the electric-field magnitude is larger for CRBC than for COBC pulses. For pulses with an even number of cycles, while the peak field magnitude is the same for both CRBC and COBC pulses, the COBC pulses show less modulations in $|E(t)|$ with time, and the probed targets are thus exposed to field values close to the peak field for a substantially longer time than is the case for the CRBC pulses. The differences between CRBC and COBC pulses become less significant as the number of optical cycles is increased, with one notable exception: The magnitude of the electric field is always more slowly varying for COBC than for CRBC pulses. This difference suggests that the ionization process induced by COBC pulses may more readily take place in an adiabatic manner with no significant coupling to bound excited states. For CRBC pulses, on the other hand, the relatively rapid modulations of the field bring the ionization process in the nonadiabatic regime, and is expected to induce coupling to excited states. These points will be discussed in more detail in Sec. III.

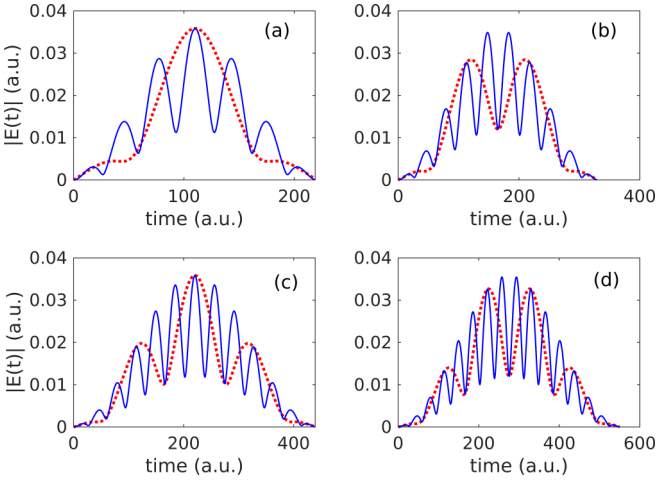

FIG. 2. Electric field magnitude, $|E(t)|=\sqrt{E_x(t)^2+E_y(t)^2}$, for COBC (dotted lines) and CRBC (solid lines) laser pulses with $1\omega-2\omega$, 1:1 intensity ratio, CEP value of $\varphi=-\pi/2$, and $N_{\rm cyc}$ equals (a) 2 cycles, (b) 3 cycles, (c) 4 cycles, and (d) 5 cycles, respectively. The peak field strength is 0.036 a.u. and the fundamental frequency corresponds to a wavelength of 800 nm.

The TDSE calculations were performed for H, Ar, Ne, and He. The single-active-electron potentials describing Ne and He were taken from Ref. [27] and for Ar from Ref. [28]. The TDSE calculations were performed for H in a radial box with size 1200 a.u. and include 8192 radial grid points and $(l_{\rm max}+1)^2$ angular basis functions, where $l_{\rm max}=50$ in the partial wave expansion of the time-dependent wave function. For each l, the azimuthal quantum number m is allowed to take values from $-l$ to l. The calculations were performed using CRBC or COBC laser pulses with $N_{\rm cyc}=2,3,4,5,10$ at laser intensities of 4.5×10^{13} W/cm^2 and 1.0×10^{14} W/cm^2. For Ar, Ne, and He, the TDSE calculations were performed in a radial box with radius 800 a.u. and include 8192 radial grid points, with $l_{\rm max}=60$ and all m's allowed for each l. Since Ar has a slightly higher ionization potential than H (ionization potentials are given later on), the TDSE calculations were performed for Ar at laser intensities (6.3×10^{13} and 1.0×10^{14} W/cm^2) in the same range as for H and including $N_{\rm cyc}=2,3,4,5,10$. For Ne and He, which have significantly higher ionization potentials than Ar and H, the calculations were performed at higher laser intensities of 1.4×10^{14}, 3.9×10^{14}, and 7.7×10^{14} W/cm^2 and $N_{\rm cyc}=2,5,10$. The results of these calculations passed convergence tests performed by changing the radial grid density and increasing the angular momentum parameters by 20%.

The PMDs ($dP/d\vec{k}$) were obtained from scattering analysis after the end of the laser pulse [29], namely, by projecting the wave packet $\psi(T)$ at the end of the laser pulse T on scattering states $\psi_{\vec{k}}^{(-)}$ of the field-free potential; see Eq. (4). The scattering states $\psi_{\vec{k}}^{(-)}$ were computed using the same potential and radial grid as used in the TDSE calculations,

$$\frac{dP}{d\vec{k}}=|\langle\psi_{\vec{k}}^{(-)}|\psi(T)\rangle|^2. \tag{4}$$

The ATI spectra were produced from the PMDs as

$$\frac{dP}{dE}=\sqrt{2E}\int_0^{2\pi}\int_0^{\pi}\frac{dP}{d\vec{k}}\sin(\theta_{\vec{k}})d\theta_{\vec{k}}d\phi_{\vec{k}}, \tag{5}$$

and the TIY was computed as the integral of the ATI spectrum or PMDs,

$$\text{TIY}=\int\frac{dP}{dE}dE=\int\frac{dP}{d\vec{k}}d\vec{k}. \tag{6}$$

As part of the analysis, the population of bound excited states was obtained at the end of the laser pulse. We also computed TIYs for H and Ar($3p$) using the weak-field asymptotic

theory (WFAT) of tunneling ionization; see Ref. [30] for a detailed presentation of the theory. Within this approach, the TIY is computed as

$$\mathrm{TIY} = 1 - \exp\left[-\int_{-\infty}^{\infty} \Gamma(t)dt\right], \tag{7}$$

where $\Gamma(t)$ is the WFAT tunneling rate. For Ar, we assume that the external field at all instants of time is aligned parallel to the lobe of the $3p$ orbital, and compute the tunneling rates based on the instantaneous magnitude of the field $|E(t)|$ as [30]

$$\Gamma(t) = \frac{\kappa|g|^2}{2}\left[\frac{4\kappa^2}{|E(t)|}\right]^{2/\kappa-1} \exp\left[-\frac{2\kappa^3}{3|E(t)|}\right], \tag{8}$$

where $\kappa = \sqrt{2I_p}$, with I_p the field-free ionization potential [$I_p = 0.58$, 0.793, and 0.90 a.u. for Ar($3p$), Ne($2p$), and He($1s$)], and g is a field-independent structure factor, $g = 2.861$, 2.406, and 2.114 for Ar, Ne, and He [31,32]. For H, by introducing the structure factor $g = \sqrt{2}$ and $\kappa = 1$ in Eq. (8), the tunneling rate reduces to $\Gamma(t) = \frac{4}{|E(t)|}\exp -[\frac{2}{3|E(t)|}]$ [30].

III. RESULTS AND DISCUSSIONS

In the first part of this section, we present the results of the TDSE calculations for H and the selected rare gases and address the effect of helicity and pulse length. In the second part, we present and discuss TIYs for H, Ar, and He based on tunneling theory for BC pulses with different pulse lengths and laser peak intensities, and compare to TDSE results. For H, we also compare the tunneling and TDSE results for the 1ω-2ω and the 1ω-3ω frequency combinations. We denote the ratio of TIYs for CRBC and COBC by $\mathcal{R}$, where

$$\mathcal{R} = \mathrm{TIY}_{\mathrm{CRBC}}/\mathrm{TIY}_{\mathrm{COBC}}. \tag{9}$$

A. TIYs of H and selected rare-gas atoms ionized by BC laser pulses: Effects of helicity and pulse duration

We compute TIYs for H and selected rare gases by solving the TDSE and show that the previously reported enhancement of TIYs for CRBC pulses (over COBC pulses) [22] depends on pulse length. The PMDs, ATI spectra, and TIYs presented in this section were computed using Eqs. (4)–(6), respectively.

We begin by presenting our TDSE results for 10-cycle pulses, where we obtain results that are consistent with recent experimental findings [22]. The resulting PMDs for H, Ar, Ne, and He are shown in Fig 3. The PMDs for Ar and Ne are incoherent sums of the contributions from the p_x and p_y orbitals, i.e., from states lying in the polarization plane of the laser field. The contribution to the TIY from the p_z orbital is negligible because the laser polarization plane is aligned parallel to its nodal plane [19,33]. From Fig. 3, we see that ionization by COBC pulses leads to PMDs with a ringlike structure, whereas a three-lobe-shaped structure superimposed on the rings is produced upon ionization by CRBC pulses. Moreover, ionization by COBC pulses leads to higher photoelectron energy compared to CRBC pulses, as was established in previous theoretical studies [2]. For ionization by CRBC pulses, an energy-dependent offset angle, with respect to the prediction of Eq. (1), can be observed in the PMDs, in particular in the PMDs for Ne and He shown in Figs. 3(g) and 3(h). The offset angle has been reported in earlier studies employing CRBC laser pulses [17,18] and was attributed to ionization time delays for electrons with different continuum energies [18]. Regarding TIYs, ionization by CRBC lasers gives enhanced TIYs compared to COBC lasers at the chosen intensities for H, He, and Ne, in agreement with recent experimental results [22]. For Ar at intensity of 6.3×10^{13} W/cm^2, the TIYs are rather similar for both CRBC and COBC laser pulses. As discussed in Ref. [22], the ratio of TIYs is very sensitive to laser peak intensity since it is caused by resonance-enhanced multiphoton ionization.

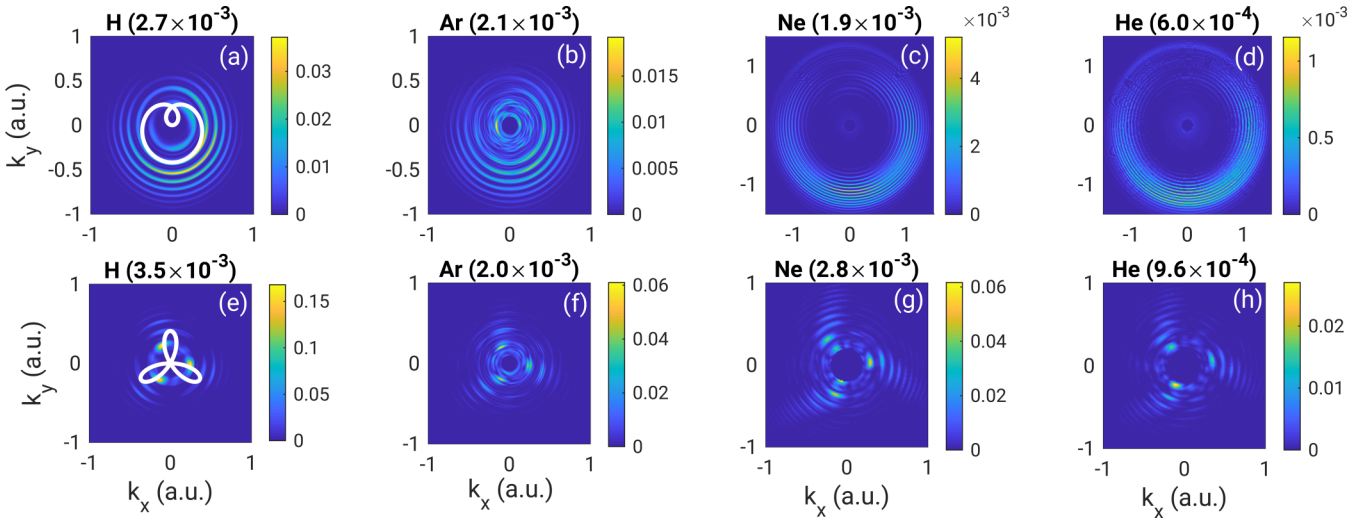

FIG. 3. PMDs with TIYs (at the top of each panel) for H, Ar, Ne, and He ionized by (a)–(d) COBC and (e)–(h) CRBC lasers with the 1ω-2ω frequency combination, 1:1 intensity ratio, a fundamental frequency corresponding to 800 nm wavelength, and $N_{\mathrm{cyc}} = 10$. The TDSE calculations for H, Ar, Ne, and He were performed at laser intensity of 4.5×10^{13}, 6.3×10^{13}, 4.0×10^{14}, and 4.0×10^{14} W/cm^2, respectively. The white curves in (a) and (e) show the predictions of the final momentum obtained from Eq. (1).

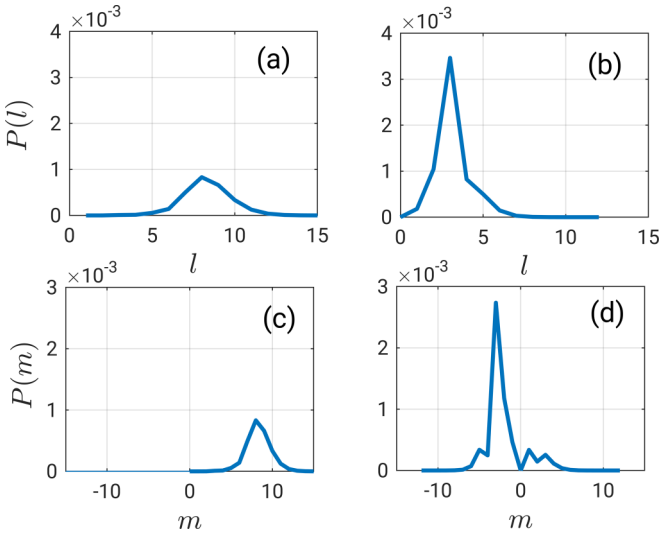

FIG. 4. The probability distributions (a), (b) $P(l)$ and (c), (d) $P(m)$ at the end of the laser pulse for the H wave packet (excluding the initial ground state) upon ionization by (a), (c) COBC pulses and (b), (d) CRBC pulses, with laser parameters given for H in Fig. 3.

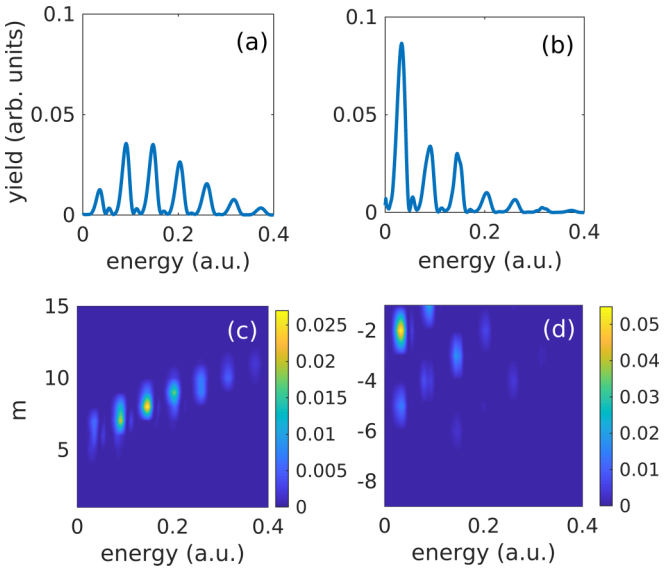

FIG. 5. ATI spectra of H ionized by (a), (c) COBC and (b), (d) CRBC bicircular laser pulses with laser parameters as in Fig. 3. In (c) and (d), we show the contributions to each ATI peak from states with different magnetic quantum number m.

From the PMDs for H in Figs. 3(a) and 3(e), we obtain TIYs of 0.0027 and 0.0035 for COBC and CRBC pulses, respectively. As a first step towards explaining the different ionization yields for CRBC and COBC, we investigated the partial wave decomposition of the wave packet, after projecting out at the initial ground state at the end of the laser pulse. We computed the probabilities of being in states with quantum numbers l and m as

$$P(l) = \sum_{|m|\leqslant l} \int_0^\infty |f_{lm}(r,T)|^2 dr \tag{10}$$

and

$$P(m) = \sum_{l\geqslant |m|} \int_0^\infty |f_{lm}(r,T)|^2 dr, \tag{11}$$

where $f_{lm}(r,T)$ is the reduced radial wave function from Eq. (2). The distributions of $P(l)$ and $P(m)$ are shown in Fig. 4 for H probed by COBC and CRBC pulses with the same laser parameters as in Fig. 3, based on analysis of the wave packet at the end of the laser pulse. Starting with distributions of $P(l)$ [see Figs. 4(a) and 4(b)], ionization by COBC leads to higher-l values. Turning to the distributions of $P(m)$ [see Figs. 4(c) and 4(d)], since the COBC pulse is left handed [the field rotates in the anticlockwise direction; see Fig. 1(a)], only states with $m > 0$ are populated; see Fig. 4(c). Since the CRBC pulse is right handed [the field rotates in the clockwise direction; see Fig. 1(b)], the laser pulse mainly populates states with $m < 0$; see Fig. 4(d). Notice that some population is found in states with $m > 0$ because the pulse is a superposition of circular fields with opposite helicities. At the present laser parameters, the $P(m)$ and $P(l)$ distributions for COBC pulses strongly resemble the one for circularly polarized lasers published in Ref. [34]. From the distributions of $P(m)$, the average m value is 8.3 for the COBC field compared to -2.8 for the CRBC field.

While the $P(m)$ distributions in Fig. 4 reveal important differences in the ionization dynamics of CRBC and COBC pulses, adding energy resolution to the discussion allows us to shed light on the role of resonances, as was proposed in Refs. [22,23]. Towards this end, we will now discuss the ATI spectra of H ionized by COBC and CRBC lasers, shown in Figs. 5(a) and 5(b) and obtained at the same laser parameters as the PMDs in Fig. 3. In the ATI spectra, the contributions to the ionization yield at each ATI peak from different magnetic quantum numbers m are shown in Figs. 5(c) and 5(d) for COBC and CRBC fields, respectively, and were computed as $\frac{dP}{dE}|_m = \Sigma_{l=m}^{l_{\max}} |\int_0^\infty \mathcal{F}_{El}(r) f_{lm}(r,T) dr|^2$, where $\mathcal{F}_{El}(r)$ is the radial wave function of the scattering state $\psi_{\vec{k}}^{(-)}$ introduced in Eq. (4).

For ionization by COBC pulses, seven peaks are observed in the ATI spectrum in Fig. 5(a), and the yield at each peak can be mapped to a specific magnetic quantum number m, as can be seen in Figs. 5(c). For example, the first ATI peak which appears at an energy of ≈0.035 has a minimum m value of 5, which corresponds to the absorption of five photons, each with energy 2ω, where $\omega = 0.057$ is the fundamental frequency. For ionization by COBC pulses, the average value of m [8.3 from Fig. 4(a)] is rather large, which suggests that ionization via "low-lying" excited states is suppressed. This conclusion is supported by the population of excited states being very small compared to the TIY; $P_{\rm ex} = 1.44 \times 10^{-5}$ compared to a TIY of 2.7×10^{-3} from Fig. 3(a).

For ionization by CRBC pulses [see Figs. 5(b) and 5(d)], the first ATI peak at an energy of ≈0.03 a.u. receives a major contribution from states with quantum number $m = -2$. The dominance of this relatively small m value suggests that the ionization into this channel could proceed via excited states. The population of excited states was computed at the end of the laser pulse, and the result shows a substantial fraction of excited-state population: $P_{\rm ex} = 2.76 \times 10^{-3}$, which is

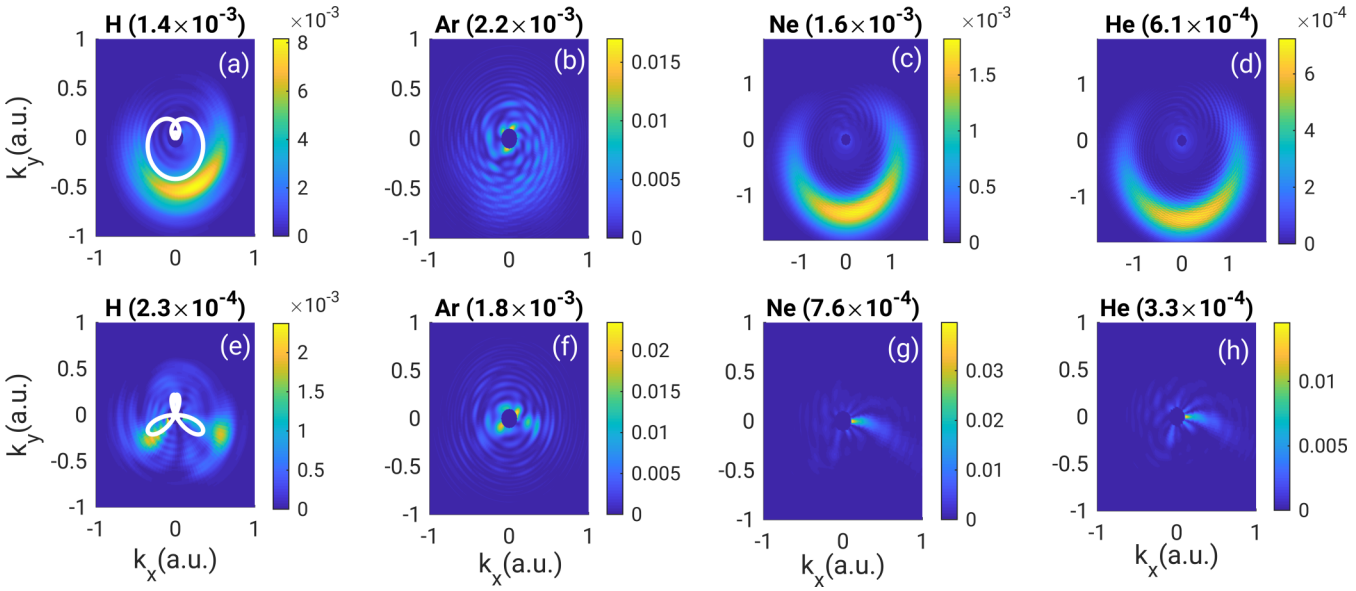

FIG. 6. PMDs with TIYs (at the top of each panel) for H, Ar, Ne, and He ionized by (a)–(d) COBC and (e)–(h) CRBC lasers with the $1\omega - 2\omega$ frequency combination, 1:1 intensity ratio, a fundamental frequency corresponding to 800-nm wavelength, and $N_{cyc} = 2$. The TDSE calculations for H, Ar, Ne, and He were performed at a laser intensity of 4.5×10^{13} W/cm^2, 6.3×10^{13} W/cm^2, 4.0×10^{14} W/cm^2, and 4.0×10^{14} W/cm^2, respectively. The white curves in (a) and (e) show the predictions of the final momentum obtained from Eq. (1).

comparable to the TIY, that is, 3.5×10^{-3} from Fig. 3(e). To identify which excited states are involved, further analysis of the wave packet at the end of the laser pulse revealed significant population in the $4f$ excited state $(l, m = 3, -3)$ located at an energy of ≈ -0.031. Notice that ionization from the $4f$ excited state via absorption of a single 800 nm photon is consistent with the position of the first ATI peak in Fig. 5(b). This suggests that ionization by CRBC pulses may indeed be enhanced by coupling to low-lying excited states, as was proposed in Ref. [22].

After having discussed the enhancement of TIYs in the long pulse limit, it is now time to address the effect of pulse length. The TDSE calculations were performed for H and the rare gases using CRBC/COBC pulses containing two cycles and keeping the other laser parameters the same as those used to obtain the results in Fig. 3. The resultant PMDs are shown in Fig. 6. The PMDs resemble the Lissajous curves of the negative vector potential for a two-cycle pulse, except for an offset angle. This is most clear for the H atom in Figs. 6(a) and 6(e). Regarding TIYs, the ratio of TIYs [$\mathcal{R}$ in Eq. (9)] is less than unity for all target atoms, which is opposite to the case for $N_{cyc} = 10$.

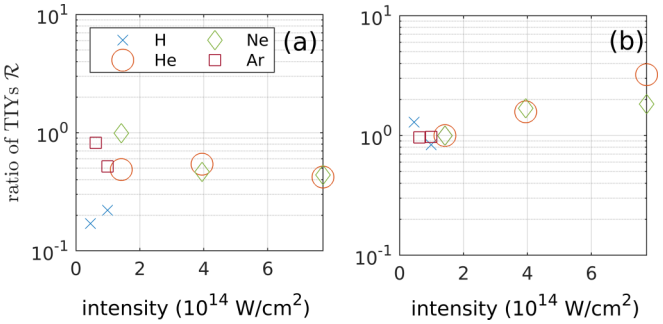

FIG. 7. Ratio of TIYs, $\mathcal{R}$ [Eq. (9)] (the scale is logarithmic), from TDSE calculations at different intensities for H, Ar, Ne, and He ionized by (a) two-cycle and (b) 10-cycle CRBC and COBC laser pulses with 1ω-2ω frequency combination and 1:1 intensity ratio. The fundamental frequency corresponds to a wavelength of 800 nm.

The ratio of TIYs for the CRBC and COBC pulses depends on laser intensity [22] due to channel-closing effects [23]. In Fig. 7, we show the effect of intensity on $\mathcal{R}$ in the short and long pulse limits, based on TIYs from TDSE calculations for H and the rare gases ionized by BC laser pulses with $N_{cyc} = 2, 10$. The TDSE calculations were performed for H at 4.5×10^{13} and 1.0×10^{14} W/cm^2, for Ar at 6.3×10^{13} and 1.0×10^{14} W/cm^2, and for both Ne and He at 1.4×10^{14}, 3.9×10^{14}, and 7.7×10^{14} W/cm^2. From Fig. 7, the ratios $\mathcal{R}$ obtained for 10-cycle pulses complement the recent experimental findings [22]. For two-cycle pulses, by contrast, a reduction of $\mathcal{R}$ is observed for H and the selected rare gases at both intensities: The maximum value of $\mathcal{R} = 0.989$ is calculated for Ne at 1.4×10^{14} W/cm^2, whereas the minimum value of $\mathcal{R}$ is 0.17 is for H at a laser intensity of 4.5×10^{13} W/cm^2.

To summarize this section, the presented results demonstrate that the ratio of TIYs for CRBC and COBC laser pulses depends on pulse duration, with pulses containing two cycles giving a different trend compared to recent findings for BC pulses containing many cycles [22]. In the next section, we will use the tunneling theory to further explore the behavior of $\mathcal{R}$ with pulse length, frequency ratio, and laser intensity.

B. TIYs from TDSE and tunneling theory

Based on the preceding discussion, the ratio $\mathcal{R}$ depends on pulse duration, with pulses containing few cycles giving results different from recent experimental findings [22] and TDSE calculations for laser pulses containing many cycles.

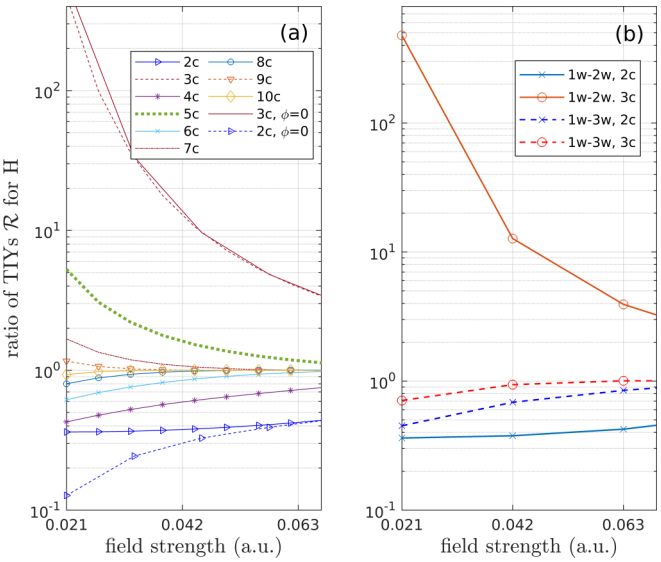

FIG. 8. (a) Ratio of TIYs $\mathcal{R}$ [Eq. (9)] (the scale is logarithmic) computed at different field strengths from tunneling theory for different pulse durations and CEP (ϕ) values. The CEP value is $\phi = -\pi/2$ unless stated otherwise. In (b), $\mathcal{R}$ is shown on a logarithmic scale for BC pulses with 1ω-2ω (solid lines) and 1ω-3ω (dashed lines) frequency combinations with $N_{\rm cyc} = 2, 3$.

To shed light on the origin of this phenomenon, tunneling rates [Eq. (8)] and the corresponding TIYs [Eq. (7)] were computed for H at laser intensities below the over-barrier intensity ($\approx 1.4 \times 10^{14}$ W/cm^2 [35]).

The ratio $\mathcal{R}$ is shown for H in Fig. 8(a) based on tunneling theory results obtained for 1ω-2ω bicircular lasers with different pulse lengths and peak field values. While the tunneling picture and corresponding TIYs are not expected to be very accurate at the considered frequencies, these results may still give us important information about the effect of pulse length and CRBC/COBC effects. From Fig. 8(a), it is seen that the ratio $\mathcal{R}$ can reach unity by increasing either the field strength or the number of optical cycles, or both. Accordingly, in the long pulse limit ($N_{\rm cyc} = 10$), tunneling theory does not predict enhancement of TIYs for CRBC lasers. For short pulses, by contrast, the enhancement of TIYs for CRBC lasers depends on the number of optical cycles, with pulses containing an odd number of optical cycles producing $\mathcal{R}$ values larger than unity, whereas pulses with an even number of optical cycles produce $\mathcal{R}$ values less than unity.

To understand the dependence of tunneling rates and corresponding TIYs on pulse length, we refer the reader to the plots of the electric fields for CRBC and COBC pulses shown in Fig. 2. For short pulses with an odd number of cycles, the peak electric field is higher for CRBC pulses than for COBC pulses, which explains why $\mathcal{R}$ is larger than unity. For short pulses with an even number of cycles, while the peak electric field has the same value for both CRBC and COBC pulses, the COBC pulses show less modulations in the magnitude of the electric field, and the probed targets are thus exposed to electric-field values close to the peak field strength for a substantially longer time, thereby increasing the TIYs for COBC pulses compared to CRBC pulses, which explains why $\mathcal{R}$ is less than unity.

Next, we compare the TIYs from tunneling theory [30,32] to the TDSE results for H, Ar, and He ionized by CRBC/COBC laser pulses with $N_{\rm cyc}$ in the range 2–10. The ratios $\mathcal{R}$ are listed for H, Ar, and He as a function of pulse duration in Table I. Although there are quantitative differences between the TIYs derived from the TDSE calculations and tunneling theory, they both agree that $\mathcal{R}$ depends on pulse duration in the sense that $\mathcal{R}$ is larger (smaller) than unity for pulses with an odd (even) number of cycles up to $N_{\rm cyc} = 4$. For pulses with $N_{\rm cyc} \geqslant 5$, the TDSE calculations indicate that $\mathcal{R}$ strongly depends on intensity, as can be seen in the case of H ionized by 10-cycle pulses, in which case changing the laser intensity from 4.5×10^{13} to 1.0×10^{14} W/cm^2 reduces the value of $\mathcal{R}$ from 1.29 to 0.84.

Let us now discuss the effect of the CEP phase on the enhancement of TIYs for COBC pulses compared to CRBC pulses. Figure 8(a) contains plots of $\mathcal{R}$ for pulses containing two and three cycles at CEP values of $-\pi/2$ and 0 rad. For pulses containing two cycles, changing the CEP from $-\pi/2$ to 0 rad reduces $\mathcal{R}$ further. The effect of CEP is less significant for pulses containing three cycles, in particular at the higher laser intensities. Hence, the TIYs determined from tunneling theory reveal no substantial effect of CEP on the ratio of TIYs ($\mathcal{R}$). These results are supported by our TDSE calculations for H. The ATI spectra and PMDs of H ionized by COBC and CRBC laser pulses containing two cycles are shown in Fig. 9 for calculations performed at a laser intensity of 4.5×10^{13} W/cm^2 and CEP values of $-\pi/2$ and 0 rad. For COBC pulses, changing the CEP has no effect on either TIY or ATI spectra [see Fig. 9(a)] and the PMD displays an overall rotation, as can be seen in Figs. 9(b) and 9(c), showing the same behavior as for H probed by a circularly polarized laser containing few cycles [16,17]. For CRBC pulses, while the impact of CEP on the ATI and TIY is very small, as can be seen in Fig. 9(d), it alters the emission pattern in the PMDs significantly; cf. Figs. 9(e) and 9(f). This is because the shape of the ionizing field for few-cycle CRBC pulses depends on the CEP. From the TIYs, we obtain almost identical ratios of TIYs ($\mathcal{R} \approx 0.17$) for both CEP values of $-\pi/2$ and 0 rad. Hence, the suppression in $\mathcal{R}$ for short BC pulses could not be attributed to CEP effects, but rather can be rationalized in terms of the tunneling picture and the shapes of the fields (Fig. 2), which are maintaining their characteristic differences while varying the CEP.

Finally, we turn the attention to Fig. 8(b), where we plot $\mathcal{R}$ as a function of field strength for 1ω-2ω and 1ω-3ω frequency combinations. The results are based on tunneling theory calculations for pulses with $N_{\rm cyc} = 2, 3$. For pulses with the 1ω-3ω frequency combination and at a field strength corresponding to intensity 4.5×10^{13} W/cm^2, we obtain $\mathcal{R}$ values of 0.63 and 0.89 for two-cycle and three-cycle pulses, respectively. This suggests that the ratio ($\mathcal{R}$) is less than unity for short pulses, regardless of the number of optical cycles. This is in contrast to results for pulses with the 1ω-2ω frequency combination, for which case the ratio $\mathcal{R}$ could be larger or smaller than unity depending on the number of cycles being odd or even, respectively.

For the two-cycle and three-cycle pulses with the 1ω-3ω frequency combination, we can understand the ratio of TIYs

TABLE I. Ratio of TIYs ($\mathcal{R}$) [Eq. (9)] for H, Ar, and He at different laser intensities and pulse durations (N_{cyc}) as obtained from TDSE calculations and tunneling theory (WFAT [30,32] results in parentheses). The intensities listed in parentheses after the atoms are given in units of W/cm^2. The external field has a 1:1 intensity ratio and a frequency ratio of 1ω-2ω, with a fundamental frequency corresponding to a wavelength of 800 nm.

N_{cyc}	H (4.5×10^{13})	H (1.0×10^{14})	Ar (6.3×10^{13})	Ar (1.0×10^{14})	He(3.9×10^{14})	He(7.7×10^{14})
2	0.17 (0.37)	0.22 (0.40)	0.82 (0.37)	0.52 (0.38)	0.54 (0.38)	0.42 (0.41)
3	1.82 (23.98)	1.28 (6.27)	1.09 (32.10)	1.39 (13.06)		
4	0.91 (0.55)	0.71 (0.66)	0.89 (0.53)	0.78 (0.59)		
5	1.31 (1.95)	0.87 (1.32)	0.99 (2.13)	1.01 (1.62)	1.22 (1.61)	1.00 (1.23)
10	1.29 (1.00)	0.84 (1.00)	0.96 (1.00)	0.97 (1.00)	1.58 (1.00)	3.22 (1.00)

based on plots of the electric fields for CRBC/COBC pulses shown in Fig. 10. For both pulses, although the peak electric field has the same value for both CRBC and COBC pulses, the COBC pulses show less modulations in the magnitude of the electric field, thereby exposing the probed targets to electric-field values near the peak field strength for a substantially longer time. This would result in increasing the TIYs for COBC pulses compared to CRBC pulses, which explains why $\mathcal{R}$ is less than unity. The tunneling results presented here are supported by the TDSE calculations for H ionized by CRBC/COBC pulses with the 1ω-3ω frequency combination, producing $\mathcal{R} = 0.6$ and 0.8 for pulses containing two and three optical cycles, respectively. The TDSE calculations were carried out at the same laser intensity and fundamental frequency used in the tunneling calculations.

IV. CONCLUSIONS

In this study, we investigated, by means of TDSE calculations, the behavior of the total ionization yields (TIYs) for the H atom and selected rare-gas atoms (Ar, Ne, and He) probed by bicircular laser pulses with counter-rotating (CRBC) and co-rotating (COBC) helicities and intensities in the range 10^{13}–10^{14} W/cm^2. We addressed the effect of pulse length on the ratio of TIYs for CRBC compared to COBC pulses, $\mathcal{R}$ [Eq. (9)]. The theoretical results revealed a strong dependence of $\mathcal{R}$ on the number of optical cycles and the frequency ratio of the combined fields. For pulses containing five or more cycles with the 1ω-2ω frequency combination, the TDSE results produce $\mathcal{R} > 1$ for most cases: That is, enhancement of TIYs for CRBC compared to COBC pulses. The enhancement of TIYs for CRBC was attributed to ionization via excited-state manifold and multiphoton ionization channels. However, there exist some cases for which there is no difference in the TIYs for CRBC and COBC pulses ($\mathcal{R} \approx 1$) or there is even a slight reduction in the TIY for the CRBC field ($\mathcal{R} \leqslant 1$) depending on laser intensity. For BC pulses with many cycles, the overall results are in agreement with recent experimental findings [22]. For BC pulses containing less than five cycles, the ratio of TIYs depends on the number of optical cycles and frequency combination. For pulses with the 1ω-2ω frequency combination, the value of $\mathcal{R}$ is larger than unity for pulses

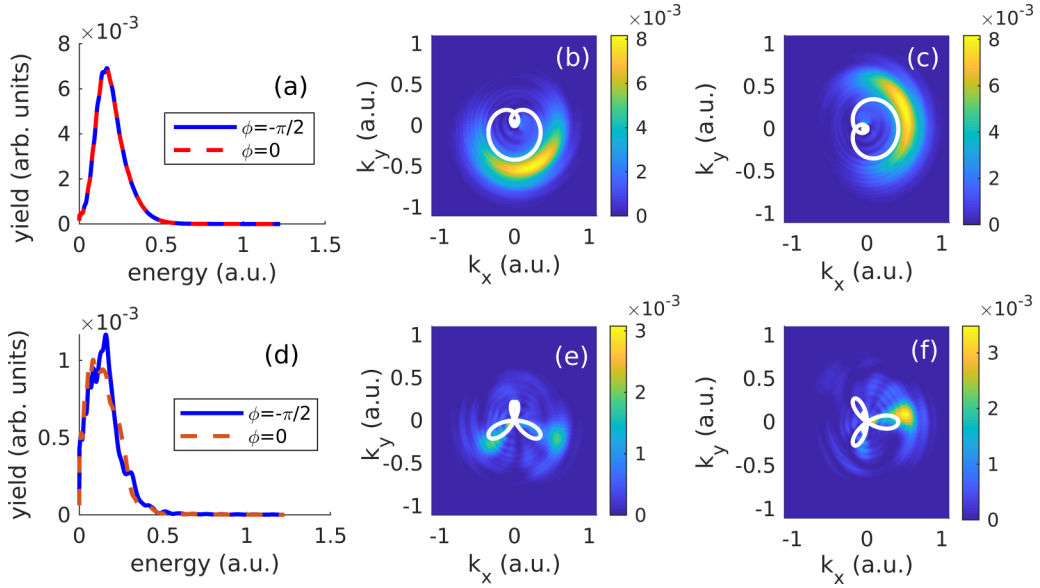

FIG. 9. Effect of CEP (ϕ) on ATI spectra and PMDs of H ionized by two-cycle (a)–(c) COBC and (d)–(f) CRBC pulses with a 1:1 intensity ratio and a 1ω-2ω frequency combination. The TDSE calculations were performed at a laser intensity of 4.5×10^{13} W/cm^2, a fundamental frequency corresponding to 800 nm wavelength, and CEP values of $\phi = -\pi/2$ in (b) and (e), and 0 in (c) and (f). The white curves denote the predictions of final momentum based on Eq. (1).

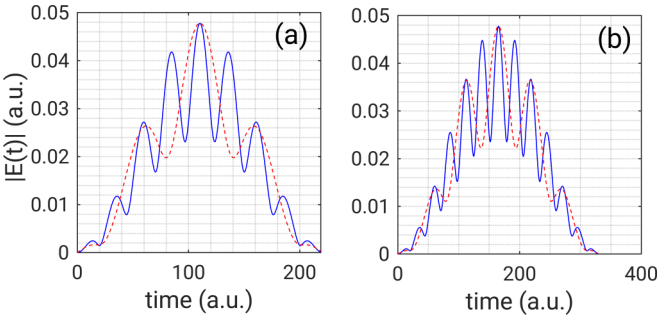

FIG. 10. Electric-field magnitude $|E(t)|$ for COBC (dashed lines) and CRBC (solid lines) laser pulses with 1ω-3ω, 1:1 intensity ratio, and N_{cyc} equal to (a) two and (b) three cycles, respectively. The peak field strength is 0.045 a.u. and the fundamental frequency corresponds to a wavelength of 800 nm.

containing an odd number of cycles, and less than unity for pulses containing an even number of cycles; see Table I. For pulses with the 1ω-3ω frequency combination, TIYs were computed for pulses containing two and three optical cycles, and for both pulse durations a $\mathcal{R}$ value of less than unity was obtained.

Calculations of the TIYs based on tunneling theory allowed us to rationalize the underlying reason for the dependence of TIYs on the pulse length in terms of the shape of the ionizing electric field: For short BC pulses containing an odd number of cycles, the peak field strength is very sensitive to helicity. For short pulses with an even number of cycles, a COBC field shows less modulations in the electric field, and the probed targets are thus exposed to field values near the peak field for a substantially longer time. The present results emphasize the role of pulse length in strong-field ionization dynamics of bicircular laser pulses, in particular in light of recent experimental observations [22].

ACKNOWLEDGMENTS

This work was supported by the Villum Kann Rasmussen (VKR) Center of Excellence, QUSCOPE, Quantum Scale Optical Processes. The numerical results presented in this work were obtained at the Centre for Scientific Computing (CSCAA), Aarhus.

[1] T. Diski, P. Sidorenko, A. Fleischer, O. Kfir, and O. Cohen, Spin angular momentum and tunable polarization in high-harmonic generation, Nat. Photon. **8**, 543 (2014).

[2] C. A. Mancuso, D. D. Hickstein, P. Grychtol, R. Knut, O. Kfir, X. M. Tong, F. Dollar, D. Zusin, M. Gopalakrishnan, C. Gentry *et al.*, Strong-field ionization with two-color circularly polarized laser fields, Phys. Rev. A **91**, 031402(R) (2015).

[3] M. Busuladžić, A. Gazibegović-Busuladžić, and D. B. Milosevic, Strong-field ionization of homonuclear diatomic molecules by a bicircular laser field: Rotational and reflection symmetries, Phys. Rev. A **95**, 033411 (2017).

[4] V.-H. Hoang, V.-H. Le, C. D. Lin, and A.-T. Le, Retrieval of target structure information from laser-induced photoelectrons by few-cycle bicircular laser fields, Phys. Rev. A **95**, 031402(R) (2017).

[5] C. A. Mancuso, K. M. Dorney, D. D. Hickstein, J. L. Chaloupka, J. L. Ellis, F. J. Dollar, R. Knut, P. Grychtol, D. Zusin, C. Gentry, M. Gopalakrishnan, H. C. Kapteyn, and M. M. Murnane, Controlling Nonsequential Double Ionization in Two-Color Circularly Polarized Femtosecond Laser Fields, Phys. Rev. Lett. **117**, 133201 (2016).

[6] S. Eckart, M. Richter, M. Kunitski, A. Hartung, J. Rist, K. Henrichs, N. Schlott, H. Kang, T. Bauer, H. Sann, L. P. H. Schmidt, M. Schoffler, T. Jahnke, and R. Dörner, Nonsequential Double Ionization by Counterrotating Circularly Polarized Two-Color Laser Fields, Phys. Rev. Lett. **117**, 133202 (2016).

[7] S. Odžak, E. Hasović, and D. B. Milošević, High-order harmonic generation in polyatomic molecules induced by a bicircular laser field, Phys. Rev. A **94**, 033419 (2016).

[8] D. Baykusheva, S. Brennecke, M. Lein, and H. J. Wörner, Signatures of Electronic Structure in Bicircular High-Harmonic Spectroscopy, Phys. Rev. Lett. **119**, 203201 (2017).

[9] D. M. Reich and L. B. Madsen, Rotating-frame perspective on high-order-harmonic generation of circularly polarized light, Phys. Rev. A **93**, 043411 (2016).

[10] D. M. Reich and L. B. Madsen, Illuminating Molecular Symmetries with Bicircular High-Order-Harmonic Generation, Phys. Rev. Lett. **117**, 133902 (2016).

[11] K. M. Dorney, J. L. Ellis, C. Hernandez-García, D. D. Hickstein, C. A. Mancuso, N. Brooks, T. Fan, G. Fan, D. Zusin, C. Gentry, P. Grychtol, H. C. Kapteyn, and M. M. Murnane, Helicity-Selective Enhancement and Polarization Control of Attosecond High Harmonic Waveforms Driven by Bichromatic Circularly Polarized Laser Fields, Phys. Rev. Lett. **119**, 063201 (2017).

[12] M. Han, P. Ge, Y. Shao, Q. Gong, and Y. Liu, Attoclock Photoelectron Interferometry with Two-Color Corotating Circular Fields to Probe the Phase and the Amplitude of Emitting Wave Packets, Phys. Rev. Lett. **120**, 073202 (2018).

[13] O. Kfir *et al.*, Generation of bright phase-matched circularly-polarized extreme ultraviolet high harmonics, Nat. Photon. **9**, 99 (2014).

[14] C. A. Mancuso, D. D. Hickstein, K. M. Dorney, J. L. Ellis, E. Hasović, R. Knut, P. Grychtol, C. Gentry, M. Gopalakrishnan, D. Zusin *et al.*, Controlling electron-ion rescattering in two-color circularly polarized femtosecond laser fields, Phys. Rev. A **93**, 053406 (2016).

[15] C. P. J. Martiny and L. B. Madsen, Finite-bandwidth effects in strong-field ionization of atoms by few-cycle circularly polarized laser pulses, Phys. Rev. A **76**, 043416 (2007).

[16] Christian Per Juul Martiny and L. B. Madsen, Symmetry of Carrier-Envelope Phase Difference Effects in Strong-Field, Few-Cycle Ionization of Atoms and Molecules, Phys. Rev. Lett. **97**, 093001 (2006).

[17] M. Abu-samha and L. B. Madsen, Probing atomic and molecular targets by intense bicircular counter-rotating laser fields, J. Phys. B **51**, 135401 (2018).

[18] H. Xie, M. Li, S. Luo, Y. Li, Y. Zhou, W. Cao, and P. Lu, Energy-dependent angular shifts in the photoelectron momen-

tum distribution for atoms in elliptically polarized laser pulses, Phys. Rev. A **96**, 063421 (2017).

[19] M. Abu-samha and L. B. Madsen, Alignment dependence of photoelectron momentum distributions of atomic and molecular targets probed by few-cycle circularly polarized laser pulses, Phys. Rev. A **94**, 023414 (2016).

[20] I. Petersen, J. Henkel, and M. Lein, Signatures of Molecular Orbital Structure in Lateral Electron Momentum Distributions from Strong-Field Ionization, Phys. Rev. Lett. **114**, 103004 (2015).

[21] S. Eckart, M. Kunitski, I. Ivanov, M. Richter, K. Fehre, A. Hartung, J. Rist, K. Henrichs, D. Trabert, N. Schlott, L. P. H. Schmidt, T. Jahnke, M. S. Schöffler, A. Kheifets, and R. Dörner, Subcycle interference upon tunnel ionization by counter-rotating two-color fields, Phys. Rev. A **97**, 041402(R) (2018).

[22] C. A. Mancuso, K. M. Dorney, D. D. Hickstein, J. L. Chaloupka, X.-M. Tong, J. L. Ellis, H. C. Kapteyn, and M. M. Murnane, Observation of ionization enhancement in two-color circularly polarized laser fields, Phys. Rev. A **96**, 023402 (2017).

[23] D. B. Milošević and W. Becker, Channel-closing effects in strong-field ionization by a bicircular field, J. Phys. B **51**, 054001 (2018).

[24] E. P. Wigner, On the behavior of cross sections near thresholds, Phys. Rev. **73**, 1002 (1948).

[25] T. K. Kjeldsen, L. A. A. Nikolopoulos, and L. B. Madsen, Solving the m-mixing problem for the three-dimensional time-dependent Schrödinger equation by rotations: Application to strong-field ionization of H_2^+, Phys. Rev. A **75**, 063427 (2007).

[26] M. R. Hermann and J. A. Fleck, Split-operator spectral method for solving the time-dependent Schrödinger equation in spherical coordinates, Phys. Rev. A **38**, 6000 (1988).

[27] X. M. Tong and C. D. Lin, Empirical formula for static field ionization rates of atoms and molecules by lasers in the barrier-suppression regime, J. Phys. B **38**, 2593 (2005).

[28] H. G. Muller and F. C. Kooiman, Bunching and Focusing of Tunneling Wave Packets in Enhancement of High-Order Above-Threshold Ionization, Phys. Rev. Lett. **81**, 1207 (1998).

[29] L. B. Madsen, L. A. A. Nikolopoulos, T. K. Kjeldsen, and J. Fernández, Extracting continuum information from $\psi(t)$ in time-dependent wave-packet calculations, Phys. Rev. A **76**, 063407 (2007).

[30] O. I. Tolstikhin, T. Morishita, and L. B. Madsen, Theory of tunneling ionization of molecules: Weak-field asymptotics including dipole effects, Phys. Rev. A **84**, 053423 (2011).

[31] L. B. Madsen, F. Jensen, A. I. Dnestryan, and O. I. Tolstikhin, Structure factors for tunneling ionization rates of molecules: General hartree-fock-based integral representation, Phys. Rev. A **96**, 013423 (2017).

[32] I.-Y. Tolstikhina, T. Morishita, and O. I. Tolstikhin, Application of the many-electron weak-field asymptotic theory of tunneling ionization to atoms, Phys. Rev. A **90**, 053413 (2014).

[33] M. Abu-samha and L. B. Madsen, Interrogation of orbital structure by elliptically polarized intense femtosecond laser pulses, Phys. Rev. A **84**, 023411 (2011).

[34] C. P. J. Martiny, M. Abu-samha, and L. B. Madsen, Counter-intuitive angular shifts in the photoelectron momentum distribution for atoms in strong few-cycle circularly polarized laser pulses, J. Phys. B **42**, 161001 (2009).

[35] I. K. Kiyan and V. P. Kraĭnov, Above-barrier ionization of the hydrogen atom in a superstrong optical field, Sov. Phys. JETP **73**, 429 (1991).